

published in *Icarus*, **188**: 35–46 (2007) — doi:
10.1016/j.icarus.2006.10.037

Velocity and Vorticity Measurements of Jupiter’s Great Red Spot Using Automated Cloud Feature Tracking

David S. Choi

Department of Planetary Sciences, University of Arizona, Tucson, AZ 85721

dchoi@lpl.arizona.edu

Don Banfield and Peter J. Gierasch

Department of Astronomy, Cornell University, Ithaca, NY 14853

and

Adam P. Showman

Department of Planetary Sciences, University of Arizona, Tucson, AZ 85721

ABSTRACT

We have produced mosaics of the Great Red Spot (GRS) using images taken by the *Galileo* spacecraft in May 2000, and have measured the winds of the GRS using an automated algorithm that does not require manual cloud tracking. Our technique yields a high-density, regular grid of wind velocity vectors that is advantageous over a limited number of scattered wind vectors that result from manual cloud tracking. The high-velocity collar of the GRS is clearly seen from our velocity vector map, and highest wind velocities are measured to be around 170 m s^{-1} . The high resolution of the mosaics have also enabled us to map turbulent eddies inside the chaotic central region of the GRS, similar to those mapped by Sada et al. (1996) and Vasavada et al. (1998). Using the wind velocity measurements, we computed particle trajectories around the GRS as well as maps of relative and absolute vorticities. We have discovered a narrow ring of cyclonic vorticity that surrounds the main anti-cyclonic high-velocity collar. This narrow ring appears to correspond to a ring surrounding the GRS that is bright in $5\text{-}\mu\text{m}$ (Terrile and Beebe 1979). It appears that this cyclonic ring is not a transient feature of the GRS, as we have discovered it in a re-analysis of *Galileo* data

taken in 1996 first analyzed by Vasavada et al. (1998). We also calculate how absolute vorticity changes as a function of latitude along a trajectory around the GRS and compare these measurements to similar ones performed by Dowling and Ingersoll (1988) using *Voyager* data. We show no dramatic evolution in the structure of the GRS since the *Voyager* era except for additional evidence for a counterrotating GRS core, an increase in velocity in the main velocity collar, and an overall decrease in the length of the GRS.

Subject headings: Jupiter, Atmospheres — Atmospheres, Dynamics

1. Introduction

The *Galileo* spacecraft began its mission in 1995 and orbited Jupiter for eight years, during which it observed the planet’s satellites, rings, and atmosphere. During the 28th orbit of *Galileo* in May 2000 (G28), the spacecraft imaged Jupiter’s Great Red Spot (GRS) with a remarkable level of detail. An observation sequence was designed to make three observations of the vortex over a span of about two hours, and resulted in one of the highest resolution images of the GRS ever created. We present mosaics of these imaging observations that were used for further data analysis. A further motivation behind our analysis was to take advantage of the high native resolution of these mosaics (~ 12 km pixel⁻¹) and use an automated cloud feature tracking technique in order to avoid the errors and disadvantages associated with cloud tracking by hand. We will describe the automated technique that we utilize and how we optimized it to return the most accurate results possible, and how we compensated for unavoidable blemishes in the images, such as the inadvertent presence of a moon shadow. We present the results of our analysis and include a discussion on techniques that we employed in order to minimize the errors associated with our analysis. We also include a discussion on how our observations fit in the context of previous imaging studies of Jovian atmospheric dynamics, and what we hope to accomplish with this technique in the future.

2. Observations

2.1. Image Processing, Mosaic Construction

Three observations of the GRS at approximately 1 hour intervals were taken during the 28th orbit of *Galileo* using the Solid State Imaging (SSI) Camera. We removed any

bad pixels present in the images and divided each image by a flat field. All images were observed using the near-IR (756 nm) filter onboard the SSI system. Although all of the images are high resolution, some images were less than ideal. Some images from the first two observations contain Europa’s shadow, and a targeting error resulted in the GRS being off-center in the images and failing to observe the northern outer edges of the GRS. (Note: Although Simon-Miller et al. (2002) state that this shadow is Io’s, we have used the JPL Solar System Simulator (space.jpl.nasa.gov) to determine that it is, in fact, Europa’s shadow.)

In addition to rectifying problems with the images, we used the NAV and NAV2 subroutines under the VICAR software package to make subtle corrections to the navigational data that accompanied each image to attain the highest level of accuracy possible for our data analysis. This data consisted of spacecraft orientation and camera pointing information such as range, subsolar point coordinates, and position angle. We used planetary limb-fitting for one of the raw images as the basis of the image navigation, and supplemented the corrections to the navigation using common points found among raw image pairs. Once all of the corrected navigational data was compiled for each image, a mosaic for each observation was constructed using MaRC (Map Reprojections and Conversions), an open-source map-making software package.¹ MaRC is designed to generate mosaics in a variety of map projections using the available navigational and camera orientation data. We built the mosaics using a simple cylindrical projection in order to facilitate the data analysis. Our set of three mosaics is 3000x1200 pixels and is centered on the GRS itself. Each mosaic spans 15 to 27 degrees south planetocentric latitude², and 12 to -18 degrees west longitude (System III). The native resolution of the mosaics is roughly 12 km pixel⁻¹. Once all of the mosaics were constructed, we made one final correction to the mosaics by dividing by the cosine of the solar incidence angle (μ_o) at the time the data were taken. In an effort to minimize manipulation to the imaging data, no further contrast enhancement was performed on the images; tests using high-pass filtered mosaics showed no systematic improvement in the final results. One of our mosaics is shown in Figure 1.

2.2. Automated Cloud Feature Tracking

Previous methods of extracting information on the atmospheric winds relied primarily on manual cloud tracking, such as that performed by Dowling and Ingersoll (1988). A

¹Interested readers can download MaRC at <http://sourceforge.net/projects/marc>

²All latitudes referenced in this paper in the text or in the figures are planetocentric unless stated otherwise.

human operator selects the same cloud feature in an image pair, and software is then used to calculate the wind velocity at that location. An automated approach removes the human selection component. We have developed an algorithm that extracts a basis portion of an image mosaic, numerous portions of a mosaic at a later time for comparison, and calculates the cross-correlation coefficient for each comparison. (See Figure 2 for an illustration.) We assume that the wind vector is then represented by the offset distance between the basis portion and the comparison portion with the highest cross-correlation score. We do not use an arbitrarily set minimum correlation score as a cutoff for eliminating candidate wind vectors and instead choose to eliminate spurious results after the tracking. This process is repeated systematically throughout the mosaic. One example of using automated tracking on *Galileo* data taken during its flyby of Venus can be found in Toigo et al. (1994).

The only user controlled parameters for this analysis are the size of the comparison box that the search algorithm uses, and the density of wind vectors for the final result that the user desires. These two parameters are distinct. It is best to use the smallest box size possible in order to minimize the position error associated with each wind vector (see the error analysis section, Section 4 for more discussion). However, if the basis image and the region surrounding it are devoid of high-contrast cloud features, the feature tracking algorithm can return inaccurate results because there may be multiple locations where the algorithm believes there is high correlation in a region featuring little contrast.

Our method of counteracting this problem is to use a relatively large comparison box initially, which maximizes the presence of distinguishing cloud features in the comparison images. The caveat here is that using a large window will result in the algorithm essentially measuring the offset between the distinguishing feature(s), which can be anywhere in the comparison image. However, the algorithm designates the location of the velocity vector to be at the exact center of the comparison image. This can lead to *position error* in the wind velocity vectors, which can cause errors in the calculation of vorticities or spatial derivatives of the flow even if the magnitude and direction of the wind vectors themselves are accurate. Therefore, in order to maximize the localization and precision of each result, we execute the correlation algorithm again, and using the initial large comparison box result as a guide (i.e. an initial guess), perform the final velocity calculation using a small comparison box. We restrict the search area for seeking the small comparison box with the highest cross-correlation score to a relatively small area (20x20 pixels, or approximately 57,600 km²) around the initial guess, effectively forcing the final velocity vector to be within some range around the initial guess. We have found this method to be especially useful in spatially resolving areas of high horizontal shear and reducing the chance that an artificially inflated value for vorticity (which depends on the value of velocity shear) will result in our later analysis. Similar techniques (of using both large and small correlation boxes) were employed

by Rossow et al. (1990) in their analysis of *Pioneer* Venus images. A discussion of the position error of our velocity vectors can be found in section 4.

One issue to mention here is the question of what box size should be used for the comparison images, both large and small. For the large box, we want to keep it as small as possible to reduce position error but maximize the chance of unique distinguishing features for each comparison throughout the mosaic. We performed a statistical analysis of the correlation scores returned for each velocity vector returned by the algorithm using the box size as the only adjustable parameter. The mean of the correlation scores increased linearly with increasing box size at first as expected. However, the mean started to approach a limit with larger box sizes as they reached a regime of diminishing returns. We selected a box size of 100x100 pixels as our large box, which is where the median correlation scores began to asymptotically approach their peak. For the small box, we use its size to directly control the density and localization of the results. This can be judged subjectively by using the smallest box size that returns as few spurious results as possible when combined with targeting from the large box results. We performed this test using small boxes of 10, 20, and 30 pixels, and each returned similar results. Thus, we selected the 10 pixel box to maximize resolution and minimize positional error.

3. Results

Since there are three mosaics, three different combinations of image comparisons were input into our feature tracking algorithm. The results shown here represent an average of the three individual comparisons. Spurious results were identified by mapping the zonal and meridional velocities from each individual comparison as a grayscale map and identifying pixels with obvious differences against the surrounding region. Although we tested several methods similar to bad pixel removal algorithms used in astronomy (in order to remove cosmic ray hits, for example) of objectively removing spurious results returned by the cloud trackers, none were consistent in removing all of the inaccurate results. Therefore, we were forced to remove the spurious results manually. It is possible that certain cloud morphologies may have yielded spurious results that appeared to be valid. However, we believe this is unlikely because the spurious results were typically found in areas of bad imaging data (near image edges, moon shadows, or other image artifacts) and that our technique of using both large and small correlation boxes reduced the possibility of this occurrence. In locations where results have been removed, we use an average of two comparisons or the only valid result. Locations with no valid data have been filled in using a nearest-neighbor averaging algorithm. Less than 1 percent of the main body of the maps had no valid results and were

filled using nearest-neighbor averaging; these areas were concentrated at or near the edges of the maps.

3.1. Wind Velocities

The feature tracking algorithm returns separate values for offset in the zonal and meridional directions. Velocities were determined using the following equations:

$$u(\lambda, \phi) = \left(x_{\text{off}}(\lambda, \phi) \times d \times \left(\frac{\pi}{180} \right) \times r(\phi) \right) / t \quad (1)$$

$$v(\lambda, \phi) = \left(y_{\text{off}}(\lambda, \phi) \times d \times \left(\frac{\pi}{180} \right) \times R(\phi) \right) / t \quad (2)$$

where u and v are zonal and meridional velocity as a function of longitude λ and planetographic latitude ϕ , respectively. x_{off} and y_{off} represent the displacements in the zonal and meridional direction in pixels, and d is degrees per pixel for the mosaics (≈ 0.01). The offsets are then converted into radians and then multiplied by the radii of curvature in the appropriate direction at that point. Radii of curvature are determined by the following equations:

$$r(\phi) = R_e (1 + \epsilon^{-2} \tan^2 \phi)^{-\frac{1}{2}} \quad (3)$$

$$R(\phi) = R_e \epsilon^{-2} \left(\frac{r(\phi)}{R_e \cos \phi} \right)^3 \quad (4)$$

where r and R are the zonal and meridional radii of curvature, respectively, as a function of planetographic latitude ϕ . The original map coordinates for the mosaics are in planetocentric latitude, and conversions are made appropriately. R_e is the equatorial radius of Jupiter, and epsilon (ϵ) is defined as the ratio of a planet's equatorial to polar radius ($R_e/R_p \approx 1.069$ for Jupiter). Finally, dividing the displacement by the time t between observations (3216 s, or twice this for the comparison between the first and last observations) yields a result for velocities in m s^{-1} . (Each observation sequence consisted of 4-6 raw images taken over a span of approximately 5 minutes, and we assume that there was no significant motion of clouds within each mosaic. In addition, the sequence was designed to keep a consistent time interval between observations for raw images covering the same area of the target.)

Figure 3 shows a summary of our results as a map of wind velocity vectors. In this figure, only a ninth (every third vector in each dimension) of the total number of vectors in our dataset are shown for the purposes of clarity. Our feature tracking technique is clearly able to resolve the GRS high-velocity collar, the relatively calm central region, and jets to the south and northwest of the GRS. We measure a maximum tangential velocity near 170 m s^{-1} along the southern edge of the GRS. Our results show agreement with previous studies: the maximum value measured using our automated techniques is consistent (in both magnitude and location of the velocity vector) with manual measurements on the G28 dataset made by Simon-Miller et al. (2002), her figure 6. However, Simon-Miller also reports velocities near or greater than 190 m s^{-1} on all sides of the high-velocity collar from her analysis. We cannot explain this inconsistency, as large navigational uncertainties would be required in our images to account for the error. We tested the possibility that the discrepancy is a result of our automated tracker failing to track very small features that are easier to track by hand and were instead returning an averaged velocity representative of the region around the small feature. However, this theory failed as tests with smaller tracking box sizes did not return systematically increased velocities in the GRS collar. Furthermore, manual cloud tracking has been employed on the G28 dataset by Legarreta and Sánchez-Lavega (2005); they report a maximum velocity in the flow collar of 180 m s^{-1} . Overall, all of the G28 maxima lie slightly higher than the maximum manual measurement ($\sim 150 \text{ m s}^{-1}$) made by Vasavada et al. (1998) on GRS imaging data from 1996, suggesting a modest increase in the strength of the velocity collar over a four-year period. However, we have analyzed the G1 imaging dataset used by Vasavada et al. (1998) and have performed a similar automated feature tracking analysis on their dataset between two of their images that are separated by nearly 1 hour. The maximum tangential velocities as measured in the G1 dataset by Vasavada manually and by this work automatically are in agreement, suggesting that our automated analysis is returning the velocities properly and that a real strengthening has occurred in that region of the collar.

Zonal and meridional velocity profiles of the GRS from our analysis are shown in Figures 4 and 5. We generate the zonal velocity profile by taking measurements within 1.5° longitude of the central meridian of the GRS in the G28 dataset (-5.8° W) and average over 0.25° bins in latitude. The meridional velocity profile is generated in a similar manner by taking measurements within 1.5° latitude of 20° South planetocentric latitude and averaging over 0.25° bins in longitude. The targeting error of the G28 observations is shown by the cutoff of the zonal velocity profile in the northern latitudes compared to profiles made by previous missions. The “double peak” at the southern end of the profile marks the strong zonal jet stream located in that region. Overall, the zonal velocity profile is similar to the profile calculated by Vasavada et al. (1998), but our analysis shows a weakening of the northern

collar countered with a strengthening of the southern collar. These differences are relatively substantial, with a 10-20 m/s difference in velocity on average (40-50 m/s difference at some latitudes) systematically across the collars that is difficult to explain with the expected uncertainty ($\sim \pm 5 \text{ m s}^{-1}$, see section 4). However, we note that Simon-Miller et al. (2002) report a strengthening of both the northern and southern GRS collar, which is inconsistent with our result.

The slight counter-rotation of the GRS core can also be seen in both velocity profiles, confirming the result derived by Vasavada et al. (1998). There is also increased wind shear in the G28 velocity profile, particularly in the southern half of the GRS between the core and the high-velocity collar. Furthermore, the G28 profile seems to be slightly asymmetrical, with the peak zonal velocity on the southern collar roughly 30 m s^{-1} higher than the highest zonal velocity on the northern collar. (Because the northernmost portion of the GRS was not captured because of a targeting error [see Figure 1], there is a possibility that somewhat higher velocities may exist farther north, but this seems unlikely given the fact that the zonal velocity profile in Figure 4 appears to begin turning over.) The asymmetry is not as pronounced for the meridional velocities, with a difference of about 10 m s^{-1} between the peak velocities on the western and eastern edge of the velocity collar.

3.2. Turbulent Eddies

The remarkable high resolution of our images enables us to map the central region of the GRS with great detail. A full-resolution wind velocity vector map of the region is shown in Figure 6. Most of the central region appears to be incoherent and turbulent, but a couple of notable features can be seen. An anti-cyclonic sub-vortex that is likely fed by the high-velocity collar can be seen to the northeast, and hints of another sub-vortex can also be seen in the southwest corner. Furthermore, the northern half of a cyclonic circuit (flowing W to E) can be seen near the geographic center of the GRS. There also appears to be a branch from the main high-velocity collar that feeds this motion. The southern half of the circuit is not clearly seen in this figure and appears to be lost in the chaotic motion. Sada et al. (1996) found a small, cyclonic vortex near the center of the GRS from their analysis of *Voyager* images, whereas Vasavada et al. (1998) found a complete cyclonic circuit surrounding the center of the GRS. The fickle nature of the velocity features in the GRS central region based on observations over a span of over 20 years only reaffirms the chaos and turbulence that likely dominate this region. The timescale over which these features change is unknown, but it is probably less than a couple of years.

3.3. Particle Trajectories

We treated the problem of integrating velocities to create particle trajectory paths as an ODE and composed an algorithm that used the velocity fields and the classical fourth-order Runge-Kutta (RK) method to solve for the trajectories. Our algorithm was written using steps outlined in *Numerical Recipes in C* (Press et al. 1992), but using IDL instead. The algorithm starts its integration with a user-controlled input point of origin. The fourth-order RK algorithm requires derivatives of the velocity fields in both horizontal directions for its calculations (i.e. a calculation of the horizontal wind shear). Because the wind shear calculated using the raw, noisy velocity data can lead to artificially inflated numbers for the shear and negatively affect later calculations, we smoothed the velocity field in a $1 \times 1^\circ$ box centered at each trajectory point, and then calculated the shear using the smoothed field. We set our smoothing functions to be velocity functions that vary only linearly in latitude and longitude. Once a new trajectory point was calculated using the integrator, the algorithm repeats the smoothing using a box centered at the new point.

Figure 7 shows our map of the representative trajectories we have selected for use in our analysis. None of the calculated trajectories yielded closed curves; in fact, all of them spiraled into the center of the GRS. We sought to investigate why the trajectories were not fully closing on themselves. We first tested our integrator on a synthetic dataset that would return a smooth, closed circle as its trajectory. Once we verified that the integrator worked properly, we added noise to our dataset that would affect the final trajectory in order to assess whether errors in the dataset or in the analysis were affecting the trajectories. We discuss the various sources of errors and how the gaps in the trajectories affect our interpretation of the results later in Section 4. However, through extensive testing of the synthetic dataset with noise, we are confident in concluding that the various sources of error in the dataset and in our analysis can only explain a small fraction of the gap in the particle trajectories. We speculate that transient eddies, i.e. a time-dependent flow that is present in the GRS high-velocity collar such as Rossby waves or other pulsations, were captured in our observations and are the reason behind the trajectories’ failure to close. Although it is a possibility that the convergence of the trajectories is a real result, it seems unlikely given that most dynamical models of the GRS predict a divergent flow over the GRS that would occur over a much longer timescale than what is seen from our trajectories (Conrath et al. 1981).

3.4. Vorticities

Relative vorticities were determined using the following equation (Dowling and Ingersoll 1988):

$$\zeta = -\frac{1}{R} \frac{\partial u}{\partial \phi} + \frac{u}{r} \sin \phi + \frac{1}{r} \frac{\partial v}{\partial \lambda} \quad (5)$$

Absolute vorticities were determined by simply adding the Coriolis parameter $f = 2\Omega \sin \phi$ to the relative vorticities. The vorticity calculation also requires the derivatives of the velocity field. We smooth the velocities over a $1 \times 1^\circ$ box centered at each velocity vector map gridpoint using the same smoothing algorithm mentioned earlier to calculate trajectories, and then use those wind shear values to calculate vorticities.

Figure 8 shows a grayscale map of relative vorticity for the Great Red Spot and surrounding region. Lighter shades indicate positive (anti-cyclonic or counter-clockwise in the southern hemisphere) vorticity whereas darker shades signify negative (cyclonic) values. It can be seen that the high-velocity collar is strongly anti-cyclonic. Curiously, the southern half of the high-velocity collar appears to have larger magnitude vorticity values compared with the northern half. However, the most interesting feature seen in Figure 8 is the ring of cyclonic vorticity that surrounds the GRS high-velocity collar. Similar rings surrounding the GRS have been observed before from $5\text{-}\mu\text{m}$ infrared spectroscopy (Flasar et al. 1981), but this observation marks what we believe to be the first such observation of a ring from a dynamical perspective. Although Dowling and Ingersoll (1988) calculated a relative vorticity map for their analysis of *Voyager* images, no clear ring of cyclonic vorticity can be seen in their figure. Our result for the relative vorticity based on the G1 dataset is also shown in Figure 8. Because the cyclonic ring is also seen in the G1 dataset, we can conclude that this feature is not transient but appears to be a distinguishing characteristic of the Great Red Spot.

Although the trajectories that we have calculated are open, we present an analysis of how absolute vorticity changes along these trajectories. The original trajectories were divided into a locus of points at 30-minute intervals along each trajectory. We then calculated the vorticity at each point using a modified version of our algorithm by performing a separate velocity smoothing around each trajectory point. (Thus, we do not perform an interpolation of the vorticity map at the selected trajectory points. Instead, we perform a separate calculation and smoothing at each point.) Three trajectories were selected for analysis, and the result is shown in Figure 9.

Potential vorticity (PV) is defined as $\frac{(\zeta+f)}{H}$ where $(\zeta + f)$ is absolute vorticity and H is a measure of the layer (or pressure) thickness of the fluid layer. This is a form of potential vorticity first developed by Ertel (1942) and also used in Dowling and Ingersoll (1988). Therefore, relative changes in the layer thickness of the rotating fluid layer can be tracked by analyzing how absolute vorticity changes along a trajectory, assuming conservation of PV.

Figure 9 generally matches the results determined by Dowling and Ingersoll (1988): layer thickness variations as a function of latitude cannot be solely attributed to the β effect (the effect of the Coriolis parameter varying with latitude). In particular, trajectory F shows a thickening of the fluid layer over a narrow range of latitudes from the distinct slope in Figure 9 compared with the slope of the Coriolis parameter f . Trajectories A and C show similarities overall in their slopes in comparison to f , but portions of the trajectories also show distinct slopes. Similar results are shown in Dowling and Ingersoll (1988), their Figure 14. One caveat to our analysis is that because the calculated trajectories spiral in towards the GRS center, our assumptions for time-independent flow and PV conservation are not entirely valid, and the effect of this spiraling will be discussed in section 4.

3.5. Shape and Aspect Ratio

Analysis by Simon-Miller et al. (2002) using photometric analysis of records dating back to 1880 and images from spacecraft flybys has shown a decrease in length of the GRS by nearly 50 percent. We wish to supplement what is known about this particular aspect of the GRS by analyzing the particle trajectories that were calculated using our data and by Dowling and Ingersoll (1988). We measured the length and width of trajectory curves from both datasets by defining two axes that spanned each trajectory curve: one placed along the latitude halfway in-between the minimum and maximum latitudes of each trajectory, and another placed along a line of longitude in a similar fashion. The distance of the line segment between the intersections of the trajectory points and the axes was then measured. We measured the length and width of the trajectory shapes from Dowling and Ingersoll (1988), their Figure 3, using an electronic reproduction of their figure and Adobe Photoshop. This reproduction and our annotations marking which trajectory shapes we measured are shown in 10. From our dataset, trajectory A was not analyzed because the upper portion of the trajectory was not calculated due to that portion of the GRS not being imaged.

Our results are summarized in Table 1. We report there is a slight increase in the aspect ratio (which we define as length divided by width) for the outermost GRS trajectories (trajectories 1-3 and B-C) between the *Voyager* and *Galileo* missions. This is somewhat surprising as a 3-5° decrease in the length of the GRS as estimated by Simon-Miller et al. (2002) over the twenty years between the missions would correspond to a decrease in the aspect ratio by around 20 to 25 percent (assuming the same width). In contrast, the aspect ratio of the trajectories seems to have decreased for the more interior trajectories (trajectories 5-8 and D), which is in step with the slow circularization of the GRS with time. However, we note that since our trajectories spiral inward, the true aspect ratios for our trajectory

curves are likely slightly smaller, and that our values represent an upper boundary. We also find that the aspect ratio of the trajectories from the *Voyager* data increases as the radius of the trajectories decreases; curiously, the opposite is true in the *Galileo* data. It is unclear if this is a manifestation of a physical change of the flow pattern and shape of the GRS or a change caused by a difference in the methods used to interpolate and smooth velocities and integrating them to get trajectories. We would also like to note a different line of evidence showing the “shrinking” of the GRS with time: Figure 5 distinctly shows a clear decrease in the length of the GRS, by measuring the distance between the peak meridional velocities on the western and eastern sides of the vortex.

4. Error Analysis

There are three main categories of error that affected our results. The first category is uncertainties in the location of the cloud features in the image mosaics. These uncertainties are introduced during image processing and mosaic creation when tiepoints (common features) used to stitch together the raw images are identified and selected. The second category is errors in the location of the velocity vectors. This error is generated by our automated cloud feature tracking algorithm. Although the velocity vectors are produced in a regular grid, the particular cloud feature that was tracked and was responsible for generating the velocity result does not necessarily correspond with the *exact* location of the velocity vector but can be slightly offset. The final category is errors made by the automated feature tracker from the inherent variability in Jupiter’s cloud morphology. If the a particular feature changes sufficiently between observations, then there is a good chance of the algorithm failing to recognize the correct feature by selecting the incorrect correlation peak and assigning an inaccurate velocity vector. Unfortunately, this type of error is difficult to quantify but can usually be recognized by spurious results returned by the algorithm. However, the short time interval between each G28 observation helped to reduce this error greatly at the expense of reduced resolution in velocities.

When tiepoints for the images were selected during mosaic construction, we ensured that the maximum uncertainty in cloud position would be less than 1 pixel by repeating the tiepoint selection process until this criterion was met. (The NAV2 subroutine under VICAR calculates tiepoint errors by performing an area correlation of the image around each tiepoint.) Thus, by reducing the uncertainty as much as possible during the mosaic creation process, we ensured that the errors in velocities calculated using our feature tracking algorithm would be kept to a minimum. We assume for the purposes of this error analysis that the overall uncertainty in cloud position is estimated to be 0.5 pixel for an entire

mosaic. We can then expect an error in cloud offsets from the feature tracker to be ~ 1 pixel on average. The error in cloud offsets is not expected to be greater than 2 pixels. Propagating a 1 pixel uncertainty in raw offset values yields an uncertainty of about ± 3.5 m s^{-1} in velocity. The maximum uncertainty in our velocity measurements is estimated to be about ± 7 m s^{-1} . Errors are dependent on the radii of curvature but do not vary by more than ± 0.2 m s^{-1} .

Another source of error is error in the *location* of the calculated velocity vectors. This error is directly controlled by the size of the feature tracking correlation box, and is also dependent on the amount of horizontal shear. While the velocity vector’s origin is assigned to be located at the center of the correlation box, the particular cloud feature that the feature tracking algorithm locks onto and uses for calculating the cloud motion can be located anywhere within the correlation box. Our choice of a 10 pixel (120 x 120 km) box is sufficient to keep the error to near ± 2 m s^{-1} using typical values for horizontal velocity shear in Jupiter’s atmosphere. If we had used a 30 pixel (360 x 360 km) box, we estimate the errors to be nearly 6 - 7 m s^{-1} . Thus, we estimate the overall error in the velocities to be typically around 4 m s^{-1} .

This error is insufficient to explain the gaps that are seen in the calculated trajectories, because we determined that the combined errors from camera pointing and the positions of the velocity vectors would be insufficient if they were distributed randomly throughout the synthetic dataset. Furthermore, we tested how the integrator would behave if the errors were correlated over a length scale similar to length scales found in the imaging dataset. We reason that it would be possible for errors to be similar in magnitude over a length scale of typical cloud features. This “correlated error” would produce a deviation in the trajectory that would constructively add, whereas randomly distributed errors would tend to contribute random-walk like behavior and would presumably produce little net effect on the trajectories. We tested our theory by performing an FFT on one of the image mosaics to create a power spectrum as a function of length. We determined that the dominant length scale for the FFT on our image mosaics was on the order of a few degrees. The phase of the FFT was then randomly scrambled and then inverted to produce a noisy image with the same length scale as the original data. This noisy image was then scaled to be in proportion with the expected error we would obtain from both camera pointing and velocity vector position error, and added to the synthetic dataset. Testing with the integrator on this experimental data resulted in minor trajectory gaps, but was not sufficient to explain the wide gaps in our original trajectories. We therefore conclude that some natural variation in the GRS velocity collar is responsible for the trajectory gaps that result in our data. We have no evidence that clouds at different heights adversely affected our results, but this could be another source for error.

Because the calculated trajectories do not fully close in on themselves, we cannot make the assumption that they are fully time-independent. Thus, conservation of potential vorticity may not be fully applicable to these trajectories because they are not true trajectories that track a single air parcel. Instead, the paths that we have calculated most likely traverse between multiple parcels. We estimate the typical gap between the starting and ending points of our trajectories to be $\sim 1^\circ$. Using the error estimation methods outlined in Dowling and Ingersoll (1988), we estimate the errors in the derived thicknesses to be at the 30% level. (For comparison, Dowling and Ingersoll (1988) calculated their error to be at around the 3% level.) Also, we would like to note that we executed the path integrator using the velocity data that we calculated using the G1 imaging dataset with similar results: all of the trajectories around the GRS failed to close by a similar margin. Although this is a non-negligible error, we remain confident that our analysis shows that the GRS has not undergone any drastic changes in its dynamics and overall structure since the *Voyager* era, and that our overall conclusions remain valid.

5. Discussion and Conclusions

It is not expected that this paper will be able to resolve the question of whether it is inherently better to use an automated cloud feature tracking system over a manual or user-controlled system, but we believe we have conclusively demonstrated that an all-automated approach can return quality results. The automated approach reduces the time required to painstakingly track clouds by hand and eye, though there is some additional time required to eliminate any spurious results. The automated method is particularly useful for returning a high-density, regular grid of velocity vectors, something that is not achievable with a manual approach that will typically result in a scattered grid of velocity vectors. Furthermore, the high-density velocity vector grid facilitates the calculation of particle trajectories and vorticities. However, the usefulness of an automated approach is most likely constrained by the native image resolution of the imaging dataset. It would be interesting to measure what minimum image resolution is necessary for an automated approach to be useful. It should also be noted that there is a cutoff in the time gap between observations where manual cloud feature tracking will become more useful. Using the feature tracking algorithm on G1 observations where the time gap between observations was 9-10 hours yielded a high percentage of spurious results and were unfit for analysis. Presumably, the cloud morphology had sufficiently evolved between those observations so that the tracking algorithm failed to recognize clouds at the later observation. However, the presence of compression artifacts in the G1 data may have negatively influenced the results as well. Overall, we conclude from our datasets that an automated analysis is ideal for high-resolution observations with

relatively short (~ 1 -2 hours) timesteps between images, whereas manual tracking is better for observations of any resolution but with much longer timesteps between observations. However, an exception for when longer timesteps are better suited for automated tracking may be for capturing subtle details such as eddy momentum fluxes (Salyk et al. 2006).

The most interesting feature that resulted from our analysis is the ring of cyclonic vorticity that surrounds the high-velocity collar of the Great Red Spot. A similar feature surrounding the high-velocity collar has been observed spectroscopically in $5\mu\text{m}$ (Flasar et al. 1981), but ours is presumably the first such observation made from a dynamical perspective. We could not conclusively find a cyclonic ring feature in the results of Dowling and Ingersoll (1988) and Sada et al. (1996); however, this feature was detected in our re-analysis of *Galileo* G1 data first analyzed by Vasavada et al. (1998). Thus, this feature is a real phenomenon and not an artifact of our dataset or our analysis techniques. We believe that it is unlikely that this feature is transient in nature, and we attribute the failure in detection from previous studies to the limitations brought by manual cloud tracking and the low resolution of past images. Thus, the structure of the Great Red Spot extending outward from its center can be summarized as a slightly cyclonic central core, a strongly anti-cyclonic high-velocity collar, and a narrow cyclonic outer ring. The outer cyclonic ring itself may not be interesting, as one could expect a cyclonic component to the vorticity of the GRS as the winds decay away from the center of the vortex. This is exemplified in Equation 4.9 from Holton (2004):

$$\zeta = -\frac{dV}{dn} + \frac{V}{R} \quad (6)$$

where ζ is relative vorticity, V is tangential velocity (defined positive), n is a radial coordinate (positive inward for the GRS), and R is radius of curvature (positive for the GRS). Thus, as the tangential velocity weakens with distance away from the GRS collar, the shear contribution of equation 6 (the first term) would make ζ negative. However, if the vortex winds decayed slowly away from the center over the length scale of the GRS, the curvature contribution of the vorticity (the second term, which is positive in this case) would dominate, and the vorticity of the GRS would gradually transition into the background vorticity of the regional flow. Thus, the narrow width and strong amplitude of the cyclonic ring signifies that the GRS winds decay rapidly with distance away from the main flow collar. It is unclear what process is forcing the ring to be remarkably narrow, especially when compared to the width of the main anti-cyclonic velocity collar. Overall, we believe the properties of the cyclonic ring around the GRS to be a useful constraint on the dynamics of the GRS.

We also hypothesize that there could be a thermally indirect circulation occurring in

the GRS, where downwelling motion is associated with a region of cyclonic vorticity; this type of circulation model was first proposed by Conrath et al. (1981). If there is downwelling motion in the cyclonic ring, it would coincide well with the observation that this region is bright in $5\ \mu\text{m}$, as heat from the Jovian interior could more readily escape through this outer ring. Because the $5\text{-}\mu\text{m}$ bright ring appears to be a stable feature around the GRS (see also Carlson and 40 colleagues (1996)), and because the exact mechanism generating this feature is unknown, it is a natural target for future studies on the stability and dynamics of the Great Red Spot. Previous numerical modeling attempts of the GRS have been successful (Cho et al. 2001) in reproducing particular features of the wind flow, but little attention has been paid to cyclonic rings in GRS modeling studies. Marcus (2004) has shown that cyclonic rings are present around White Oval-like vortices in his numerical studies. Furthermore, Showman (2006) has demonstrated that cyclonic rings form around Jovian anticyclones as a secondary result of his study testing the hypothesis that the zonal jets on Jupiter are powered by thunderstorms. Thus, we believe that investigating this new ring feature requires a numerical modeling approach in an attempt to reconcile it with previous GRS models and in order to understand how the properties of the Jovian atmosphere and the GRS generate this feature and regulate its width and amplitude.

Although our analysis of vorticity change along trajectories is imperfect because of the failure of the trajectories to close on their point of origin, our analysis strongly suggests that the structure of the Great Red Spot remains largely unchanged from the *Voyager* era. Our velocity measurements confirm the strengthening of the high-velocity collar since the *Voyager* era, and even since four years prior to the G28 observations, but not to the extent previously measured by Simon-Miller et al. (2002). Nevertheless, we hope to employ our automated feature tracking techniques to other high-resolution imaging datasets in the future in order to supplement our knowledge on the solar system’s diverse planetary atmospheres.

This paper benefited from the helpful comments and reviews made by Dr. Anthony del Genio and an anonymous reviewer. We thank Dr. Aswhin Vasavada for providing his projected *Galileo* G1 imaging data for analysis, and we would also like to thank Dr. Tim Dowling for providing his results from *Voyager* imaging analysis for comparison. We thank Ossama Othman for the development and use of his MaRC map projection software while at Cornell University. This work was supported by NASA’s Planetary Atmospheres Program and by Cornell Presidential Research Scholars.

REFERENCES

- Carlson, R., 40 colleagues, 1996. Near-Infrared Spectroscopy and Spectral Mapping of Jupiter and the Galilean Satellites: Results from Galileo's Initial Orbit. *Science* 274, 385–388.
- Cho, J. Y.-K., de la Torre Juárez, M., Ingersoll, A. P., Dritschel, D. G., 2001. A high-resolution, three-dimensional model of Jupiter's Great Red Spot. *Journal of Geophysical Research* 106, 5099–5106.
- Conrath, B. J., Flasar, F. M., Pirraglia, J. A., Gierasch, P. J., Hunt, G. E., 1981. Thermal structure and dynamics of the Jovian atmosphere. II - Visible cloud features. *Journal of Geophysical Research* 86, 8769–8775.
- Dowling, T. E., Ingersoll, A. P., 1988. Potential vorticity and layer thickness variations in the flow around Jupiter's Great Red Spot and White Oval BC. *Journal of Atmospheric Sciences* 45, 1380–1396.
- Ertel, H., 1942. Ein neuer hydrodynamischer Wirbelsatz. *Meteor. Z.* 59, 277–281.
- Flasar, F. M., Conrath, B. J., Pirraglia, J., Clark, P. C., French, R. G., Gierasch, P. J., 1981. Thermal structure and dynamics of the Jovian atmosphere. I - The Great Red Spot. *Journal of Geophysical Research* 86, 8759–8767.
- Holton, J. R., 2004. *An Introduction to Dynamic Meteorology*, 4th Edition. Elsevier Academic Press.
- Legarreta, J., Sánchez-Lavega, A., 2005. Jupiter's cyclones and anticyclones vorticity from Voyager and Galileo images. *Icarus* 174, 178–191.
- Marcus, P. S., 2004. Prediction of a global climate change on Jupiter. *Nature* 428, 828–831.
- Press, W., Flannery, B., Teukolsky, S., Vetterling, W., 1992. *Numerical Recipes in C: The Art of Scientific Computing*. Cambridge University Press.
- Rossow, W. B., del Genio, A. D., Eichler, T., 1990. Cloud-tracked winds from Pioneer Venus OCPP images. *Journal of Atmospheric Sciences* 47, 2053–2084.
- Sada, P. V., Beebe, R. F., Conrath, B. J., 1996. Comparison of the Structure and Dynamics of Jupiter's Great Red Spot between the Voyager 1 and 2 Encounters. *Icarus* 119, 311–335.
- Salyk, C., Ingersoll, A. P., Lorre, J., Vasavada, A. R., Ewald, S., del Genio, A. D., 2006. Interaction between Eddies and Mean Flow in Jupiter's Atmosphere: Analysis of Cassini Imaging Data. *Icarus*, in press.

- Showman, A. P., 2006. Numerical simulations of forced shallow-water turbulence: effects of moist convection on the large-scale circulation of Jupiter and Saturn. *Journal of Atmospheric Sciences*, submitted.
- Simon-Miller, A. A., Gierasch, P. J., Beebe, R. F., Conrath, B., Flasar, F. M., Achterberg, R. K., the Cassini CIRS Team, 2002. New Observational Results Concerning Jupiter's Great Red Spot. *Icarus* 158, 249–266.
- Terrile, R. J., Beebe, R. F., 1979. Summary of historical data - Interpretation of the Pioneer and Voyager cloud configurations in a time-dependent framework. *Science* 204, 948–951.
- Toigo, A., Gierasch, P. J., Smith, M. D., 1994. High resolution cloud feature tracking on Venus by Galileo. *Icarus* 109, 318–336.
- Vasavada, A. R., Ingersoll, A. P., Banfield, D., Bell, M., Gierasch, P. J., Belton, M. J. S., Orton, G. S., Klaasen, K. P., Dejong, E., Breneman, H. H., Jones, T. J., Kaufman, J. M., Magee, K. P., Senske, D. A., 1998. Galileo Imaging of Jupiter's Atmosphere: The Great Red Spot, Equatorial Region, and White Ovals. *Icarus* 135, 265–275.

Dataset	Trajectory	Aspect Ratio
<i>Voyager</i>	1	2.038
	2	1.999
	3	2.020
	4	2.075
	5	2.143
	6	2.249
	7	2.336
	8	2.467
	9	2.678
	10	3.076
<i>Galileo</i>	B	2.179
	C	2.178
	D	2.043

Table 1: Aspect ratios (length/width) for selected trajectories from the *Voyager* imaging data (Dowling and Ingersoll 1988) and *Galileo* data. The trajectories are illustrated in Figures 7 and 10.

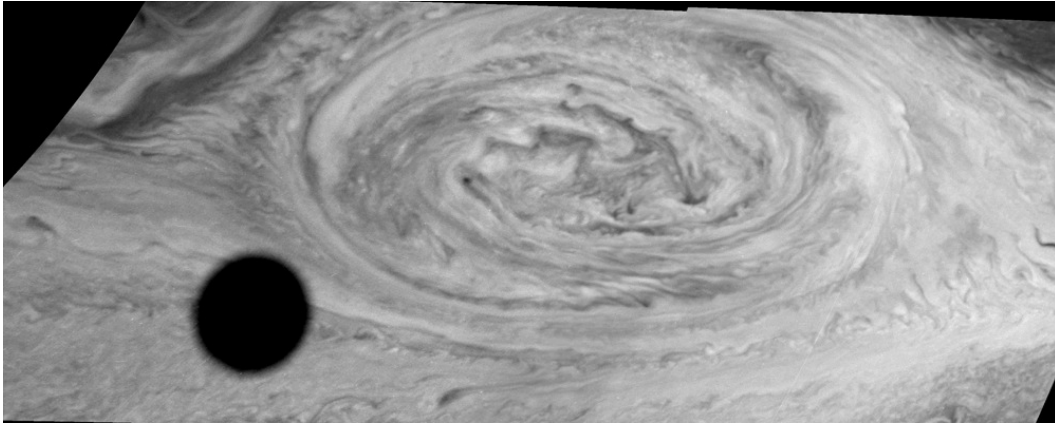


Fig. 1.— One of the mosaics analyzed by our feature tracker. The shadow in the mosaic belongs to Europa.

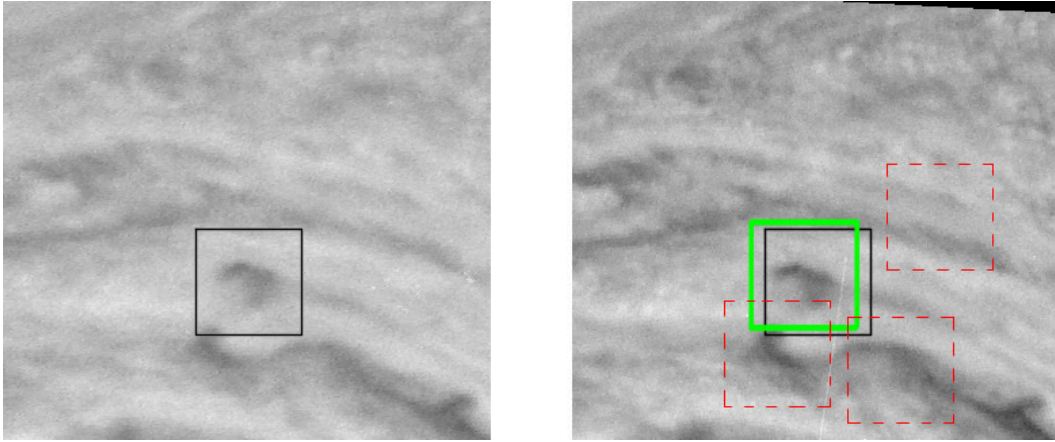


Fig. 2.— Illustration depicting how our feature tracking algorithm works. The code extracts a basis portion of an image at some initial time (left). Then, it extracts numerous comparison portions from the image at a later time (right), and calculates the one with the highest cross-correlation score (light gray, right) and rejects those with lower cross-correlation scores (dashed boxes, right). The offset distance between the light gray box and the black box is the basis for the calculation of wind velocities.

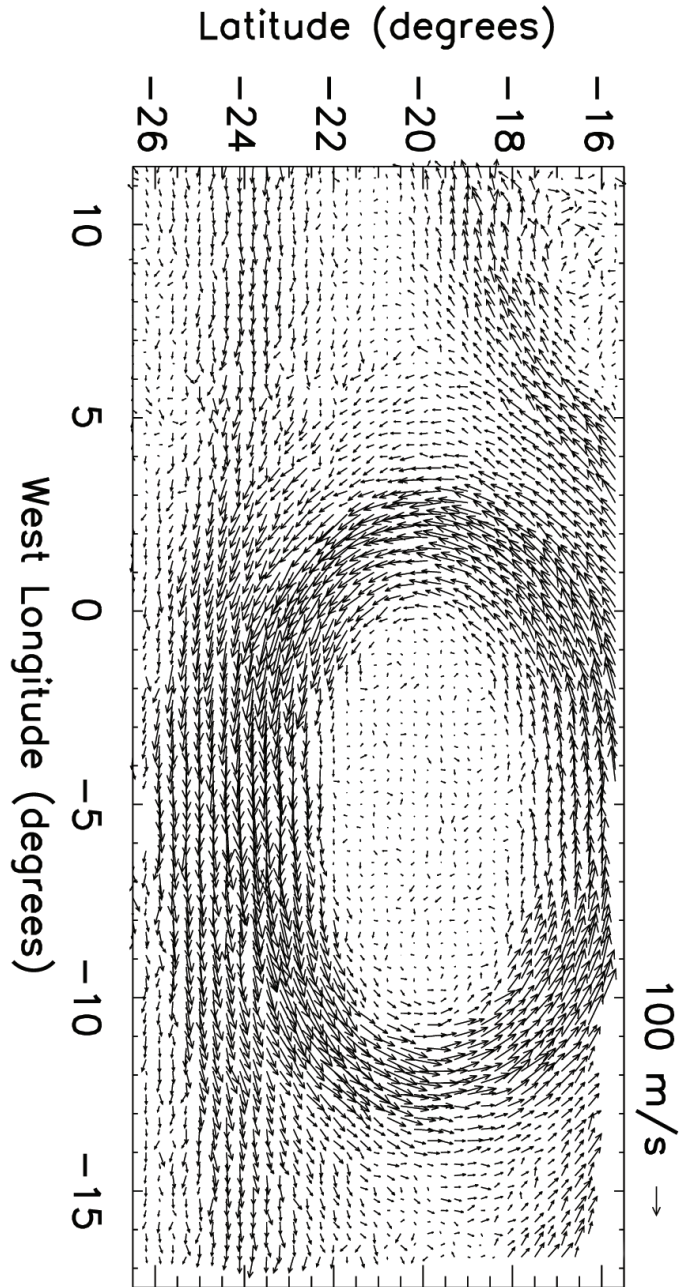


Fig. 3.— Wind velocity vector maps of the GRS and surrounding region. Only a ninth of the total number of velocity vectors calculated using our technique are shown in this figure for the sake of clarity. Note the scale vector at top right.

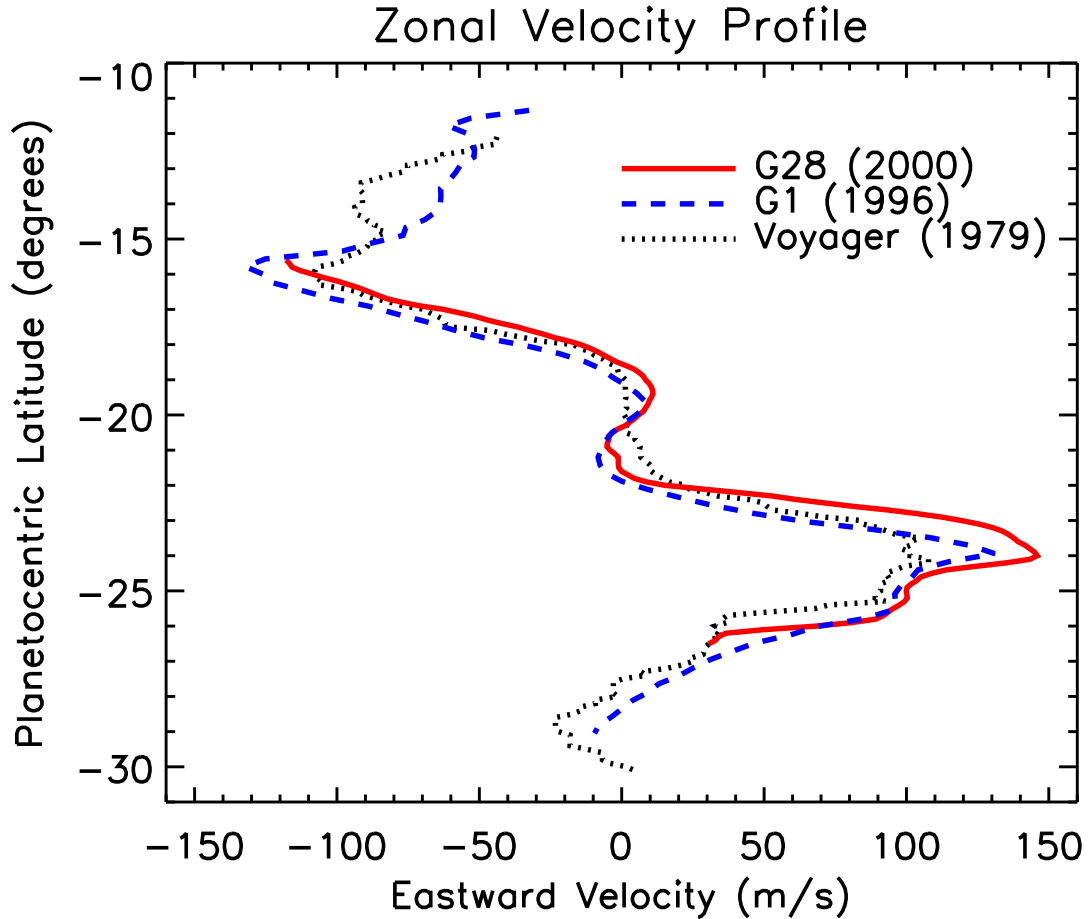


Fig. 4.— Zonal velocity profile of the Great Red Spot. The solid, red line is calculated from our *Galileo* data. Our measurements within 1.5° of the GRS central meridian were averaged over 0.25° latitude bins. The zonal velocity profile from Vasavada et al. (1998) (whose velocity profile was calculated in the same manner) is shown for comparison as a dashed, blue line. The dotted, black line is *Voyager* data from Dowling and Ingersoll (1988), where we have converted their data into planetocentric latitude and averaged their data over 1° latitude bins.

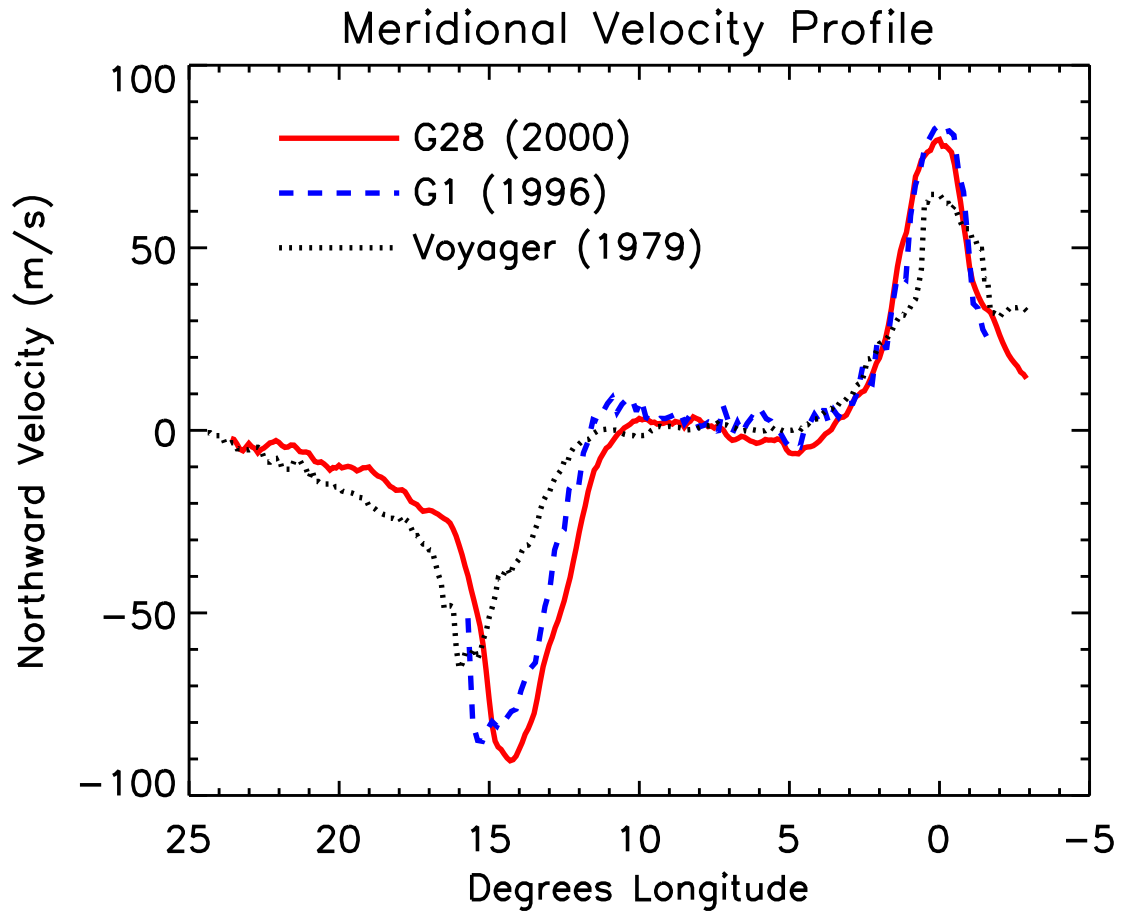


Fig. 5.— Same as Figure 4, but showing a meridional velocity profile of the Great Red Spot. Measurements within 1.5° of 20° S were averaged over 0.25° longitude bins for the G28 and G1 data, and over 1° longitude bins for the *Voyager* data. The axis for longitude is provided as a scale reference; each profile’s zero longitude was set at the peak northernmost velocity on the eastern side of the GRS.

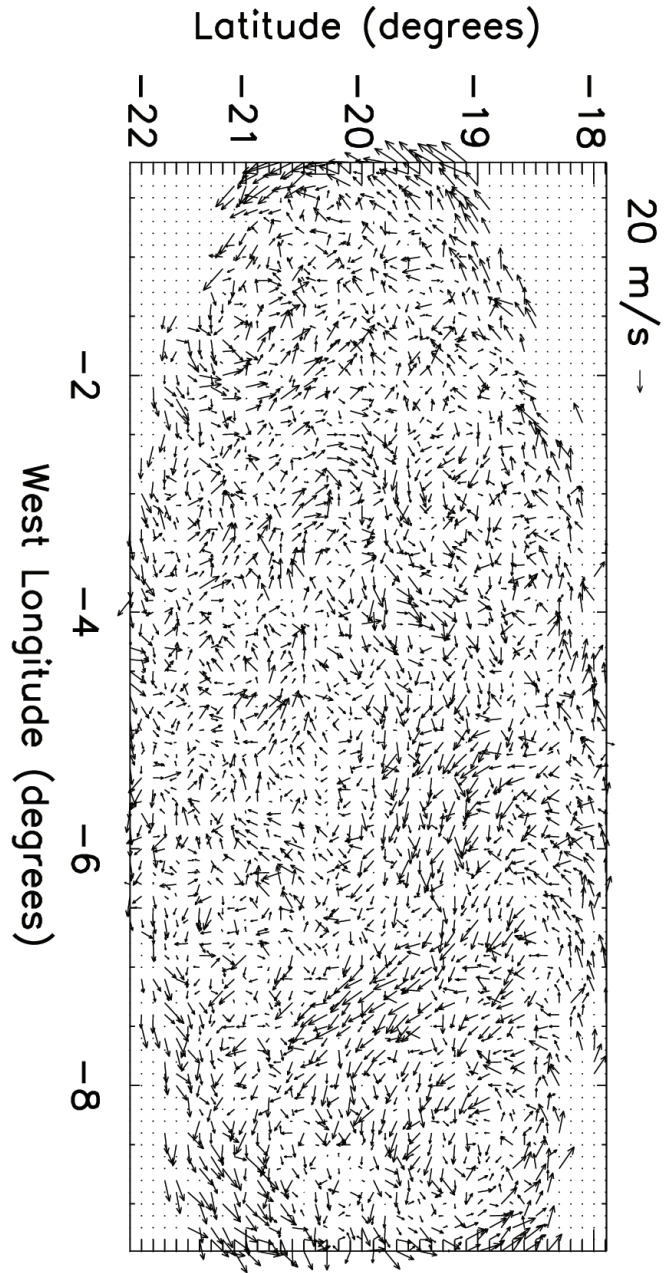


Fig. 6.— Wind velocity vector maps of the center of the GRS. All velocity vectors in our dataset are shown for highest resolution. Note the scale vector at top left.

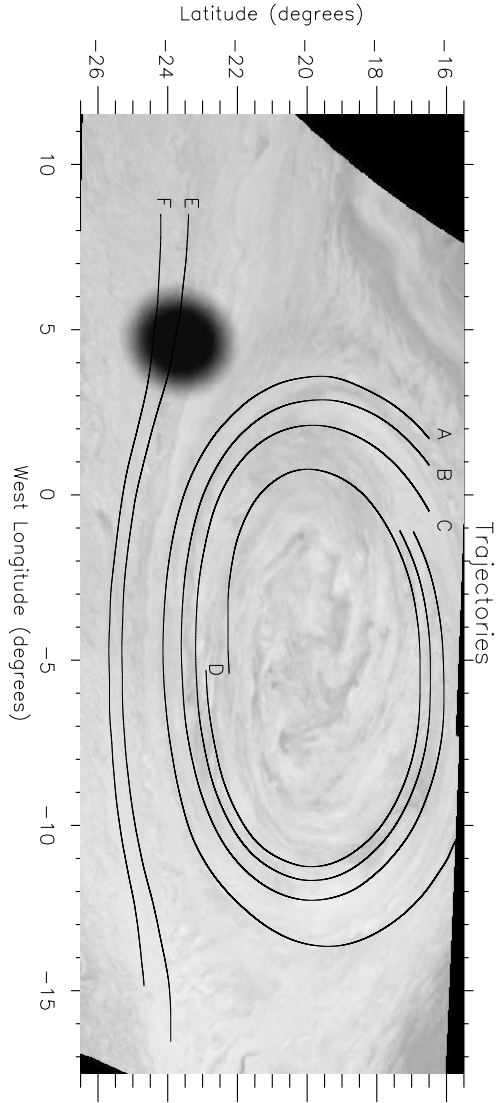


Fig. 7.— Map of particle trajectories used for analysis, overlain on one of the G28 image mosaics.

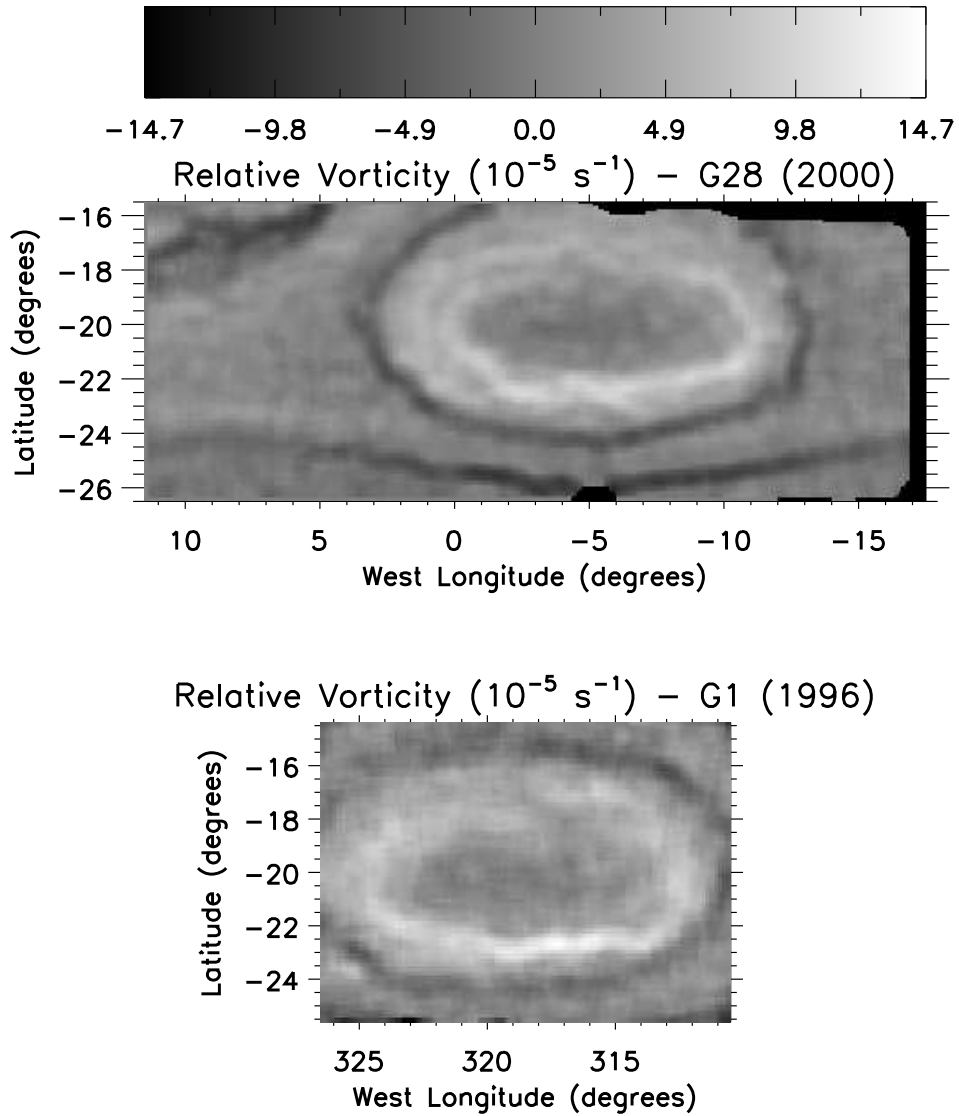


Fig. 8.— Grayscale map of relative vorticity for the Great Red Spot from the G28 and G1 datasets. Vorticity is mapped in units of 10^{-5} s^{-1} . The Great Red Spot is in the southern hemisphere of Jupiter; thus positive values denote anti-cyclonic (counter-clockwise) motion, while negative values signify cyclonic (clockwise) motion.

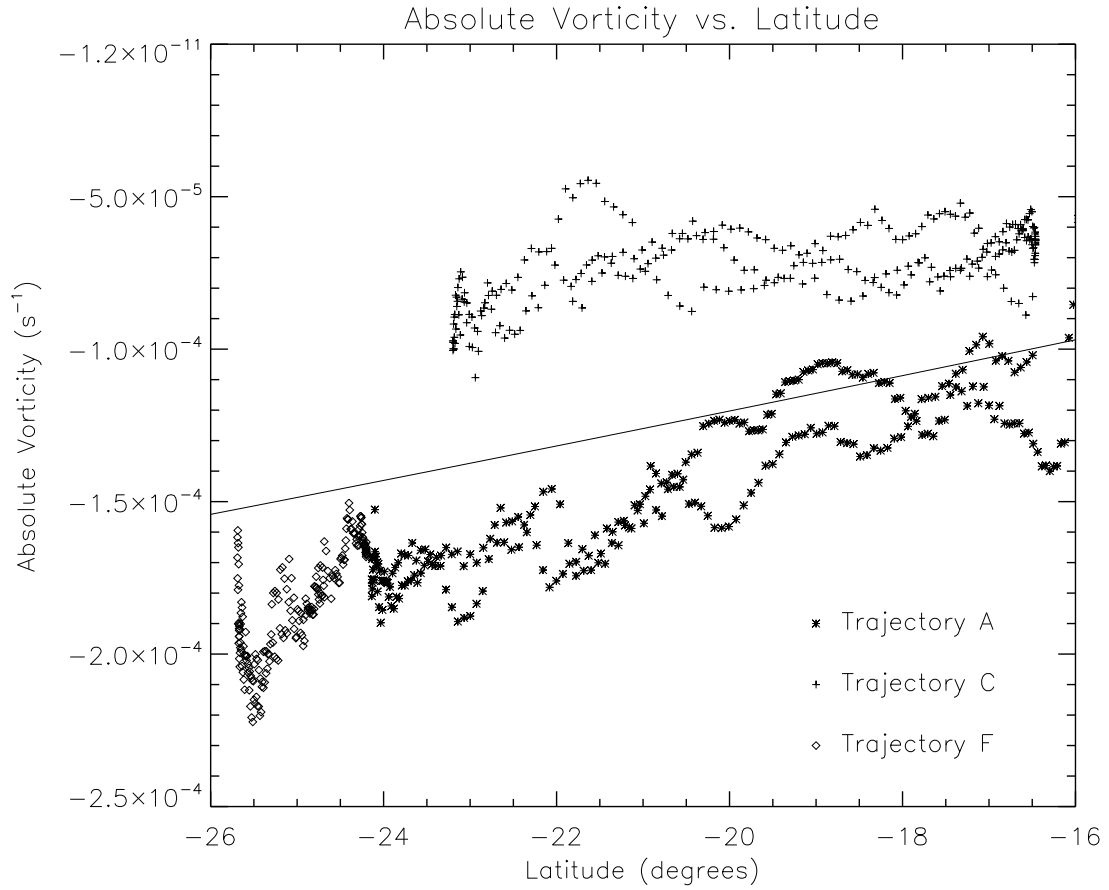


Fig. 9.— Plot of absolute vorticity ($\zeta + f$) as a function of latitude along three trajectories. The different plot symbols shown in the figure correspond to different trajectories depicted in Figure 7. The solid line corresponds to the Coriolis parameter f .

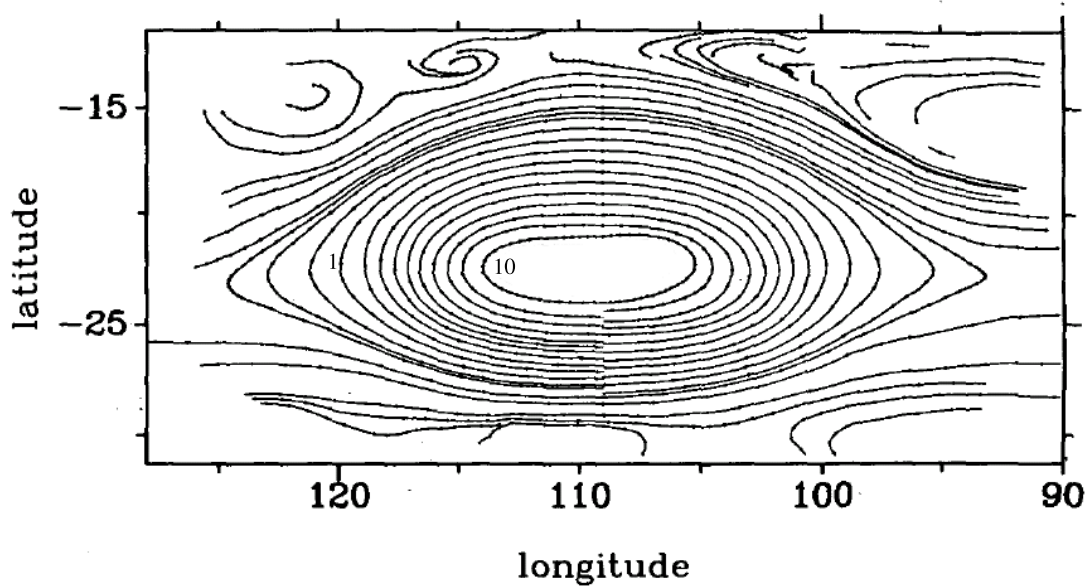


Fig. 10.— Reproduction of Figure 3 from Dowling and Ingersoll (1988), showing trajectories calculated from *Voyager* imaging data. We have added an annotation marking which trajectories were studied for this project: trajectory 1 is to the right of the numeral in the figure, and trajectory numbers increase sequentially with decreasing trajectory radius, up to trajectory 10, the inner-most trajectory depicted above. (For the purposes of clarity, we have digitally erased a trajectory that was interior to trajectory 10 and not analyzed.)